Petroleum Science 22 (2025) 4809–4822

Contents lists available at ScienceDirect

Petroleum Science

journal homepage: www.keaipublishing.com/en/journals/petroleum-science

Original Paper

An intelligent micro-nano capsule green hydrogel decorated with carbon quantum dots with delayed crosslinking characteristics for enhanced oil recovery in harsh reservoir

Chuan-Hong Kang, Ji-Xiang Guo *, Zheng-Hao Zhang, Wyclif Kiyingi, Peng-Cheng Xue

Unconventional Petroleum Research Institute, China University of Petroleum, Beijing, 102249, China

ARTICLE INFO

Article history:
Received 7 February 2025
Received in revised form
7 May 2025
Accepted 17 September 2025
Available online 23 September 2025

Edited by Min Li

Keywords:
Carbon quantum dots
Intelligent response
Green hydrogel
Delayed crosslinking
Enhanced oil recovery

ABSTRACT

Hydrogels are widely used in reservoir flow control to enhanced oil recovery. However, challenges such as environmental contamination from conventional crosslinkers, poor solubility of crosslinking agents, and short gelation times under high-temperature conditions (e.g., 150 °C) have hindered their practical application. Herein, we present the synthesis of amine-functionalized carbon quantum dots (NH_2-CQDs), which act as both a nano-crosslinker and a nano-reinforcing agent within hydrogel systems. The NH_2-CQDs-incorporated hydrogel can remain stability for 300 days under the conditions of a mineralization degree of 2.11×10^4 mg/mL and 170 °C, and has high tensile strength (371 kPa), good toughness (49.6 kJ/m^3), excellent viscoelasticity ($G' = 960$ Pa, $G'' = 460$ Pa) and shear resistance. In addition, NH_2-CQDs adds many hydroxyl groups to the hydrogel, which can be attached to the surface of various substances. At the same time, micro-nano capsules containing NH_2-CQDs were formed by self-assembly of hydrophobic SiO_2 on water droplets, the NH_2-CQDs solution is encapsulated in a capsule, and when stimulated by external conditions (temperature, pH, surfactant), the capsule releases the NH_2-CQDs solution, this method greatly delays the crosslinking time between polymer and crosslinker at high temperature. Under the condition of 170 °C and pH = 7, the gelation time of 10% hydrophobic SiO_2 coated hydrogel is 44 times that of uncoated hydrogel, which can be effectively used for deep formation flow control, and CQD give hydrogels fluorescence properties that can be used for underground signal tracking.

1. Introduction

Hydrogels are soft materials with three-dimensional (3D) cross-linked networks (Yang, 2022). The network structure of hydrogels is formed by covalent bond interaction and non-covalent bond interaction, covalent bond is mainly formed by dehydration condensation and transamidation reaction, and non-covalent bond interaction mainly includes physical entanglement, hydrogen bond, hydrophobic interaction, supramolecular interaction, electrostatic interaction and coordination interaction (Guimarães et al., 2021; Guo et al., 2020; Nele et al., 2020; Park et al., 2021; Rahmani and Shojaei, 2021; Yang et al., 2020; Yao et al., 2020; Yu et al., 2021b; Yuk et al., 2022). Therefore, hydrogels are widely used in biomedicine (Bertsch et al., 2023; Li et al., 2012; Moura et al., 2023), biomimetic smart materials (Wirthl et al., 2017; Zhang et al., 2021; Zhu et al., 2023), underground flow control (Edwards and Celia, 2018; Olasolo et al., 2016; Su et al., 2022; Sun et al., 2013; Zhang et al., 2020a), electrochemistry (Cao et al., 2023; Li et al., 2022; Miao et al., 2021). However, traditional hydrogels are still difficult to meet the functions of special requirements. To enhance the performance of hydrogels, nanoparticles have been introduced to give hydrogels more functional properties, such as optical, thermal, electrical, magnetic, mechanical and chemical properties. Nanocomposite hydrogels have been widely used in biomedicine (Clasky et al., 2021; Jiang et al., 2020; Xue et al., 2022), sensing (Ding et al., 2020; Pan et al., 2023; Zeng et al., 2025), energy technology (Mu et al., 2022; Xu et al., 2022; Yang et al., 2022), environment (Campea et al., 2021; Jayakumar et al., 2020; Yu et al., 2021a). For example, in recent hydrogel studies, by incorporating carbon quantum dots

* Corresponding author.
E-mail address: guojx003@126.com (J.-X. Guo).
Peer review under the responsibility of China University of Petroleum (Beijing).

https://doi.org/10.1016/j.petsci.2025.09.032

into the hydrogel, the hydrogel showed high sensitivity and reversibility to pH under ultraviolet light (Wang et al., 2024a).

Carbon quantum dots (CQDs) are a new type of nanomaterial with a size of less than 10 nm (Kou et al., 2020), compared with other nanoparticles, CQDs has high photostability (Li et al., 2021), low cost (Đorđević et al., 2019), good biocompatibility (Đorđević et al., 2022), high water solubility, and adjustable photoluminescence (Li and Gong, 2022). There are a large number of functional groups on the surface of CQD, including carboxyl group, amino group and aldehyde group. This structure motif not only gives CQDs high water solubility, but also makes it an ideal class of building blocks for hydrogels, and CQDs can interact with gels through various non-covalent interactions (Wang et al., 2023). Therefore, the incorporation of CQDs into hydrogels is a valuable technique for the preparation of hydrogel composites with distinctive characteristics and unique properties, which gives them great potential applications. But unfortunately, although CQDs is widely used in hydrogels, hydrogels for underground flow control are rarely reported. On the one hand, most hydrogels do not have temperature and salt resistance and cannot withstand the high temperature and high salt conditions underground. On the other hand, most of the CQDs added to hydrogels as a kind of nano-reinforcing material do not undergo chemical reactions with other components and do not fully utilize the large number of functional groups contained on the surface of CQDs, this limits the application of CQDs incorporation into hydrogels in underground flow control. In this paper, our work shows an introduction of an amino group (–NH_2) to modify CQD synthesized from glucose precursors. During CQD preparation and modification, we use glucose as a precursor and functionalize these precursors by treating them with a solution of 3-2-aminoethyl-aminopropyl trimethoxy-silane (KH-792). The covalent bonds induced by the modification of glucose precursors by KH-792 ensure that the surface of CQD prepared by them has accessible amino functional groups, thus facilitating the transamidation of NH_2-CQDs with PAM to form a hydrogel. Compared with the existing enhanced oil recovery hydrogels, in order to improve the stability of the existing hydrogels under high-temperature and high-salt conditions, in addition to the crosslinking agent, additional reinforcing agents (such as nano-silica, etc.) are often added (Liu et al., 2017; Lu et al., 2023; Yang et al., 2021), and in practical applications, the injection of hydrogels has strict limitations on the size of the reinforcing agents. NH_2-CQDs has the dual functions of both nano-crosslinking agents and nano-reinforcing agents. The crosslinking density of hydrogels and the enhancement of mechanical strength can be achieved merely by adjusting the concentration of NH_2-CQDs. Meanwhile, the size of NH_2-CQDs is not limited by practical applications and these have expanded the application of NH_2-CQDs hydrogels in the field of underground flow control for enhanced oil recovery. In order to slow down the transamidation reaction rate between NH_2-CQDs and PAM under high temperature conditions, the intelligent response micro-nano capsules coated with NH_2-CQDs solution were prepared by using hydrophobic SiO_2 as the capsule coat. The capsule was stimulated by external conditions to release NH_2-CQDs solution, and then reacted with PAM to form hydrogel. Greatly increasing the gelation time of hydrogel is conducive to the hydrogel entering deeper into the formation and improving the flow control effect.

2. Experimental section

2.1. Materials

Non-ionic polyacrylamide (PAM), molecular weight 1.2×10^7 Da, industrial grade, Henan Tianheng Water Purification Materials Co., LTD. Acrylamide, potassium persulfate, D-glucose, 3-2-aminoethyl-aminopropyl trimethoxy-silane, analytically pure, Shanghai Maclin Biochemical Technology Co., LTD.; The experimental water was oilfield formation water with salinity of 2.11×10^5 mg/L.

2.2. Synthesis of NH_2-CQDs

The synthesis and preparation process of amine functionalized CQDs is shown in Fig. 1(a). Dissolve 5.4 g of glucose in 48 mL of water, stir for 10 min, then transfer the solution to a flask and preheat it in an oil bath at 60 °C for 10 min, subsequently, add 6 mL of KH-792 and react for 4 h until the solution turns brown. After the reaction was completed, the solution was naturally cooled to room temperature and the NH_2-CQDs solution was obtained by dialysis for 24 h with a 1000 Mw dialysis bag in 1 L of water to remove the unreacted substances.

2.3. Preparation of intelligent micro-nano hydrogels

The gel preparation process is as follows: A certain amount of formation water from the oilfield site is weighed, acrylamide is added and stirred thoroughly until dissolved and NH_2-CQDs solution and polyacrylamide are slowly added using an electric stirrer at a rotational speed of 500 rad/min, finally, potassium persulfate is added and stirred evenly to obtain the NH_2-CQDs hydrogel solution. The NH_2-CQDs hydrogel was obtained by gelation at 140 °C and was named PANC hydrogel. The preparation of intelligent micro-nano-gels involves adding hydrophobic SiO_2 to NH_2-CQDs aqueous solution at a mass ratio of 1:10 to the warring high-speed stirrer and stirring at 3000 r/min for 5 min to obtain micro-nano capsules and the micro-nano-capsules are then added to AM and potassium persulfate solutions, finally, polyacrylamide was added to obtain the intelligent micro-nano capsule hydrogel.

2.4. Characterization of NH_2-CQDs and NH_2-CQDs hydrogels

The morphology and size of NH_2-CQDs were characterized by transmission electron microscopy (TEM) (FEI-TALOS-F200X) and Nanoparticle Size Analyzer (Malvern NanoZS90). Surface analysis of NH_2-CQDs and hydrogels was performed by X-ray photoelectron spectroscopy (Thermo Kalpha). The Fourier transform infrared (FTIR) spectrum of the sample was recorded at room temperature using the Thermo Nicolet IS5 FTIR spectrometer. The morphology of hydrogels was observed by scanning electron microscopy (SEM) (Quanta 200F, FEI). The spatial Raman distribution of hydrogel was obtained by using Thermo Fischer DXR Raman imaging microscope at 532 nm excitation laser wavelength. The distribution of free water, intermediate water and bound water in hydrogel was determined by low field nuclear magnetic resonance (LF NMR) (MesoMR23-060H-I) spectroscopy. Differential scanning calorimetry of hydrogels was performed using a differential scanning calorimeter (METTler Toledo DSC3, Switzerland). The ultraviolet absorption spectrum was tested with an ultraviolet–visible spectrophotometer (Shimadzu UV3600). The PL decay curve and quantum yield (QY) were analyzed with a steady-state and transient-state fluorescence spectrometer (FLS1000, Edinburgh Instruments, Edinburgh, U.K.). See Supporting Materials for analytical methods.

2.5. Evaluation of mechanical properties of hydrogels

The hydrogel samples were tested using an electronic universal testing machine (MTS, E43.10, USA) by means of tension and

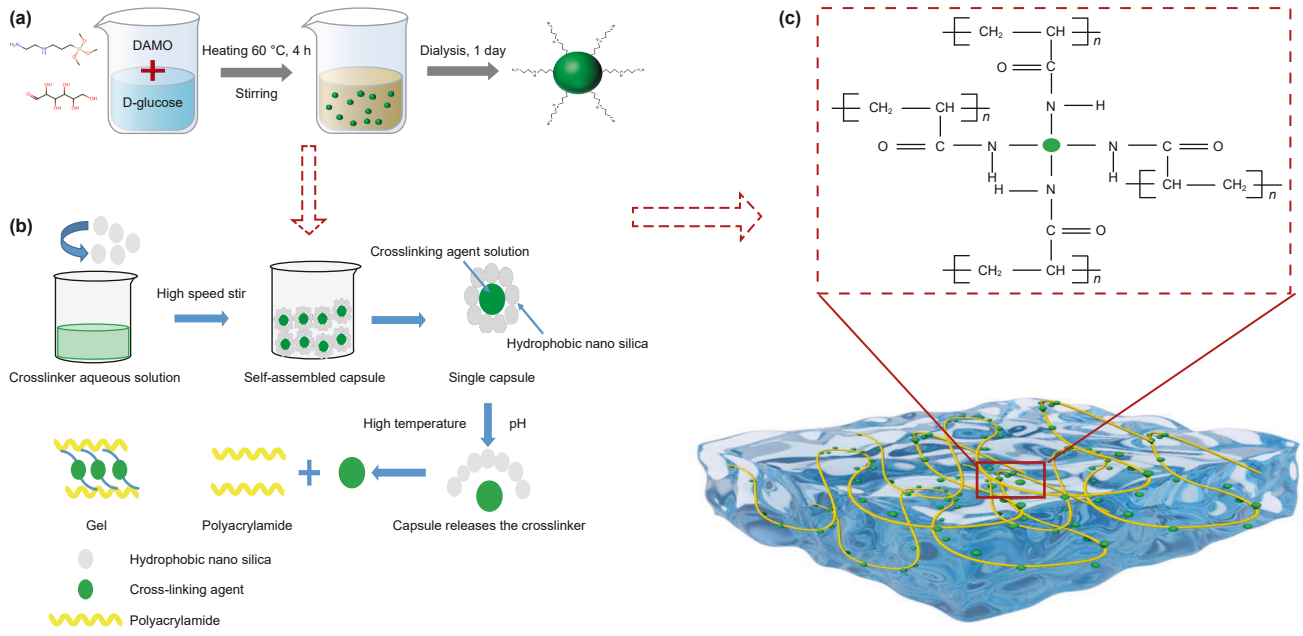

Fig. 1. Schematic diagram of CQDs synthesis with amine functionalization and preparation of intelligent micro and nano hydrogels.

compression at a rate of 5 mm/min. Hydrogel samples for tensile and compression testing are prepared in sizes of 60 × 10 × 4 mm^3 and 10 × 10 × 4 mm^3.

2.6. Evaluation of rheological properties of hydrogels

The rheological properties of the gel were measured by a HAAKE Mars III rheometer. The linear viscoelastic modulus (storage modulus G' and loss modulus G'') and creep recovery properties of the gel were all measured by the parallel flat plate system of the rheometer. At the scanning frequency of 0.1 Hz, the changes of the storage modulus G' and loss modulus G'' of hydrogel were measured in the range of 0.1–100 Pa by stress scanning. A stress value was selected in the linear viscoelastic region and set as the test stress (usually 1 Pa), and the changes of the storage modulus G' and loss modulus G'' were measured at different frequencies (0.01–1 Hz). Creep/recovery test the creep time is 100 s, the recovery time is 100 s, and the stress varies according to the different gel settings (generally 40 Pa). The critical failure point of hydrogel, that is, the intersection point of the storage modulus curve (G') and the loss modulus curve (G'') during the increase of strain, the strain range is 0.1%–5000%. Multi-period strain oscillation scanning is used to test the self-healing performance of the gel, and the high shear failure strain lasts for 600 s (elastic modulus $G1'$), and the low shear failure strain lasted for 100 s (elastic modulus $G2'$). The above tests were conducted at 25 °C.

2.7. Microscopic visual modulation and drive experiment

Microscopic oil displacement experiments were carried out using laser etched glass model, and the experimental equipment includes laser etched glass model, microscope, micropump and observation device. The experimental equipment is shown in Fig. S1 (Supplementary data), and the specific steps are listed in detail in the supplementary materials.

3. Results and discussion

3.1. Characterization of NH_2-CQDs

As shown in Fig. 2(a), the synthesized CQDs are spherical particles with good size distribution. The size of the quantum dots in TEM was statistically analyzed, and the particle size of the synthesized quantum dots was 2.5 ± 0.5 nm (Fig. 2(b)). Fig. 2(c) shows that the DLS particle size distribution of quantum dots in deionized water is 2.9 ± 0.4 nm, which is slightly larger than the size observed in TEM because the surface of CQDs is grafted with short chains containing ammonia. Fig. 2(d) shows the infrared absorption spectrum (FTIR) of CQDs. The absorption peaks of 3420 and 1645 cm^{-1} come from O–H and C=O stretching vibrations, respectively. The absorption peak at 1566 cm^{-1} comes from the bending vibration of N–H. The tensile and bending vibration peaks of C–H come from 2920 to 1385 cm^{-1}. The wide absorption peak near 1115 cm^{-1} is caused by Si–O tensile vibration. The FTIR spectral data confirmed that the surface of the synthesized CQDs contained functional groups with amino groups, which confirmed the synthesis mechanism of CQDs discussed above.

To further analyze the chemical composition of CQDs, X-ray photoelectron spectroscopy (XPS) was used to analyze it. Fig. 2(e) shows that CQDs contains Si, C, O and N elements, and the atomic proportions of the four elements can be estimated to be 8.45 %, 42.65%, 17.39% and 7.32%, respectively, based on their peak areas. The content of C atom as the core component of CQDs and the main component of the grafting chain is the highest, while the content of Si and N atom as the surface grafting part of quantum dots is relatively low. Fig. 2(f) shows that the XPS of C 1s is divided into three peaks at 284.8, 286.0 and 287.9 eV, corresponding to the C–C/C–H, C–N and C=O keys respectively. The two peaks of XPS of N 1s shown in Fig. 2(g) at 399.5 (74.1%) and 401.0 eV represent Amine (C-NR_2) and protonated amine, respectively. The peaks of O 1s shown in Fig. 2(h) at 531.3, 532.4 and 534.0 eV correspond to C=O, Si–O and C–O respectively. In Fig. 2(i), the XPS of Si 2p at 102.6 eV corresponds to siloxane (Si–O–Si). The presence of Si and

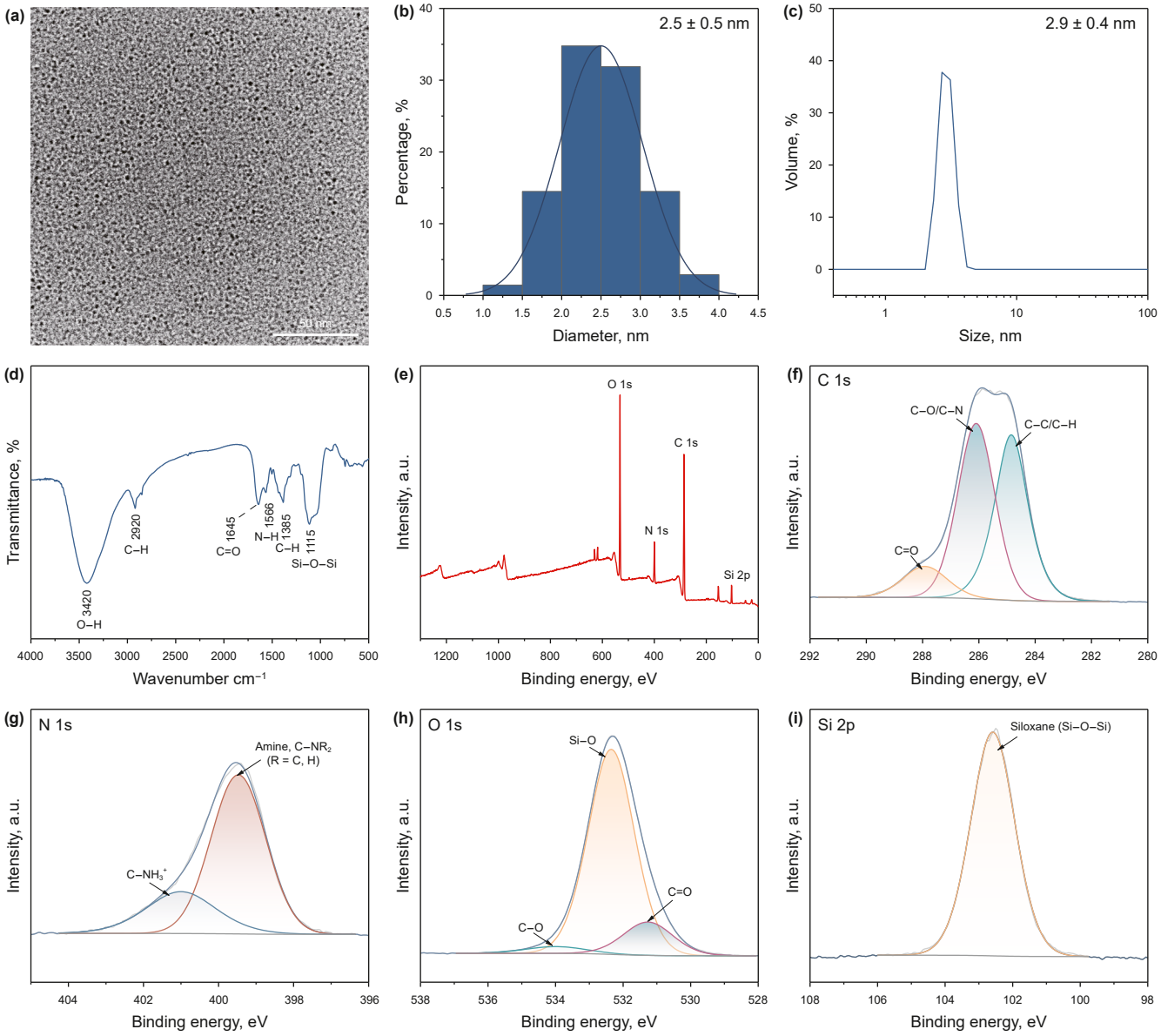

Fig. 2. **(a)** High-resolution TEM images of CQDs, **(b)** CQDs particle size distribution in TEM, **(c)** DLS particle size distribution map of CQDs, **(d)** infrared spectrogram of CQDs, **(e)** XPS spectra of CQDs, **(f–i)** fitted C 1s, N 1s, O 1s and Si high-resolution XPS spectra.

N elements indicates that in this experiment, $H_2N(CH_2)_2NH(CH_2)_3Si$ was grafted as a whole on the surface of CQDs.

3.2. Characterization of hydrogels

The infrared spectra of polyacrylamide, NH_2-CQDs, and NH_2-CQDs hydrogels are shown in Fig. 3(a), and the FTIR spectra of polyacrylamide are shown in the red curve. At 3337 and 3195 cm^{-1}, the antisymmetric expansion vibration of NH_2 and the symmetric expansion vibration of NH_2 are primary amide (–CO–NH_2). The absorption peaks near 2929 and 2851 cm^{-1} are attributed to the symmetric and antisymmetric stretching vibration of CH_2. 1651 cm^{-1} is everywhere the stretching vibration of primary amide C=O, C–N–H bending vibration of secondary amide at 1546 cm^{-1}. The peak at 1445 cm^{-1} is the CH_2-bending vibration absorption peak on the polyacrylamide main chain. The stretching vibration at 1303 cm^{-1} is –COO–; The peak near 1182 cm^{-1} is attributed to C–C tensile vibration. The peak at 1118 cm^{-1} is attributed to C–C stretching. The peak at 1040 cm^{-1} is attributed to C–N stretching vibration. The above absorption peaks are characteristic peaks of polyacrylamide. Compared with NH_2-CQDs, the characteristic peak of NH_2-CQDs-based hydrogels –OH group showed a redshift from 3402 to 3415 cm^{-1}, which was due to the interaction between NH_2-CQDs and PAM. The Si–O peak at 1108 cm^{-1} and the stretching vibration of primary amide C=O everywhere at 1651 cm^{-1} moved towards the low wave number due to transamidation reaction confirmed the cross-linking reaction between polyacrylamide and NH_2-CQDs.

The composition and surface chemical state of NH_2-CQDs hydrogel (PANC) were characterized by XPS test. The XPS spectra of NH_2-CQDs, PAM and PANC are shown in Fig. 3(b), in which Si element of NH_2-CQDs is also detected in PANC, which proves the successful reaction of NH_2-CQDs with PAM, and Na element is contained in the formation water with high salinity used in the preparation of hydrogel solution. At the same time, the peak strength ratio of C 1s to O 1s in PANC (0.68) was significantly lower

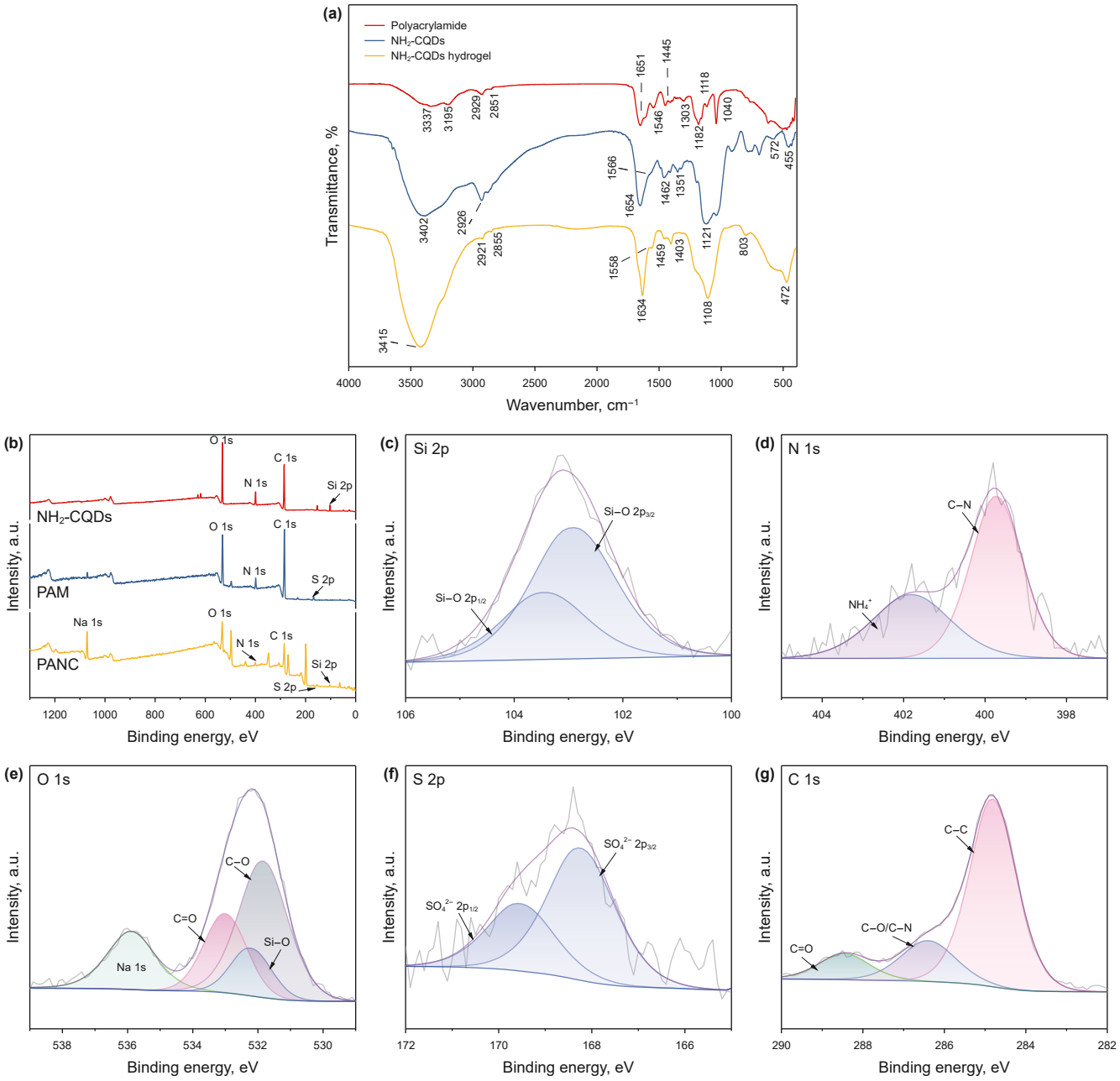

Fig. 3. (**a**) Infrared spectrum, (**b**) XPS full spectrum, (**c**) Si 2p of NH_2-CQDs hydrogels, (**d**) N 1s of NH_2-CQDs hydrogels, (**e**) O 1s of NH_2-CQDs hydrogels, (**f**) S 2p of NH_2-CQDs hydrogels, (**g**) C 1s of NH_2-CQDs hydrogels.

than that of PAM (1.08), indicating that the introduction of NH_2-CQDs produced more oxygen-containing functional groups, which was beneficial to the formation of more hydrogen bonds in the gel network (Qiu et al., 2022). The high-resolution spectrum of Si 2p, N 1s, O 1s, S 2p, and C 1s is shown in Fig. 3(c)–(g). The spectrum of Si 2p in Fig. 3(c) shows two characteristic peaks at 102.9 and 103.4 eV, which are assigned to Si–O $2p_{3/2}$ and Si–O $2p_{1/2}$, respectively. N 1s in Fig. 3(d) shows two characteristic peaks at 399.72 and 401.81 eV, corresponding to C–N and NH_4^+, respectively. The presence of NH_4^+ proves the ammonia molecule generated by the transamidation reaction between NH_2-CQDs and PAM. The O 1s spectrum in Fig. 3(e) shows four characteristic peaks at 531.8, 532.2, 533 and 535.9 eV, corresponding to C–O, Si–O, C=O and Na 1s in PANC, respectively. Si–O in PANC proves that NH_2-CQDs has combined with PAM. In Fig. 3(f), the S 2p spectrum shows two characteristic peaks at 168.2 and 169.5 eV, which are assigned to SO_4^{2-} $2p_{3/2}$ and SO_4^{2-} $2p_{1/2}$, respectively. In Fig. 3(g), the C 1s spectrum shows three characteristic peaks at 284.8, 286.4 and 288.45 eV, corresponding to C–C, C–O/C–N, C=O, respectively.

We conducted a series characterization of hydrogel cross-linking density for hydrogels (PANC) synthesized with different NH_2-CQDs contents. Fig. 4(a)–(d) is the SEM image, where Fig. 4(a) is the SEM image of PAM, and the PAM has a loose network structure and large pores. SEM images of the hydrogel synthesized with NH_2-CQDs (Fig. 4(b)) of 1 mg/L show that the microstructure of the hydrogel has a tighter network structure and no large pores compared with PAM, which is the result of the cross-linking reaction between NH_2-CQDs and PAM to form a three-dimensional network structure. SEM images of hydrogels synthesized by NH_2-CQDs and NH_2-CQDsat 3 mg/L (Fig. 4(c)) and 5 mg/L (Fig. 4

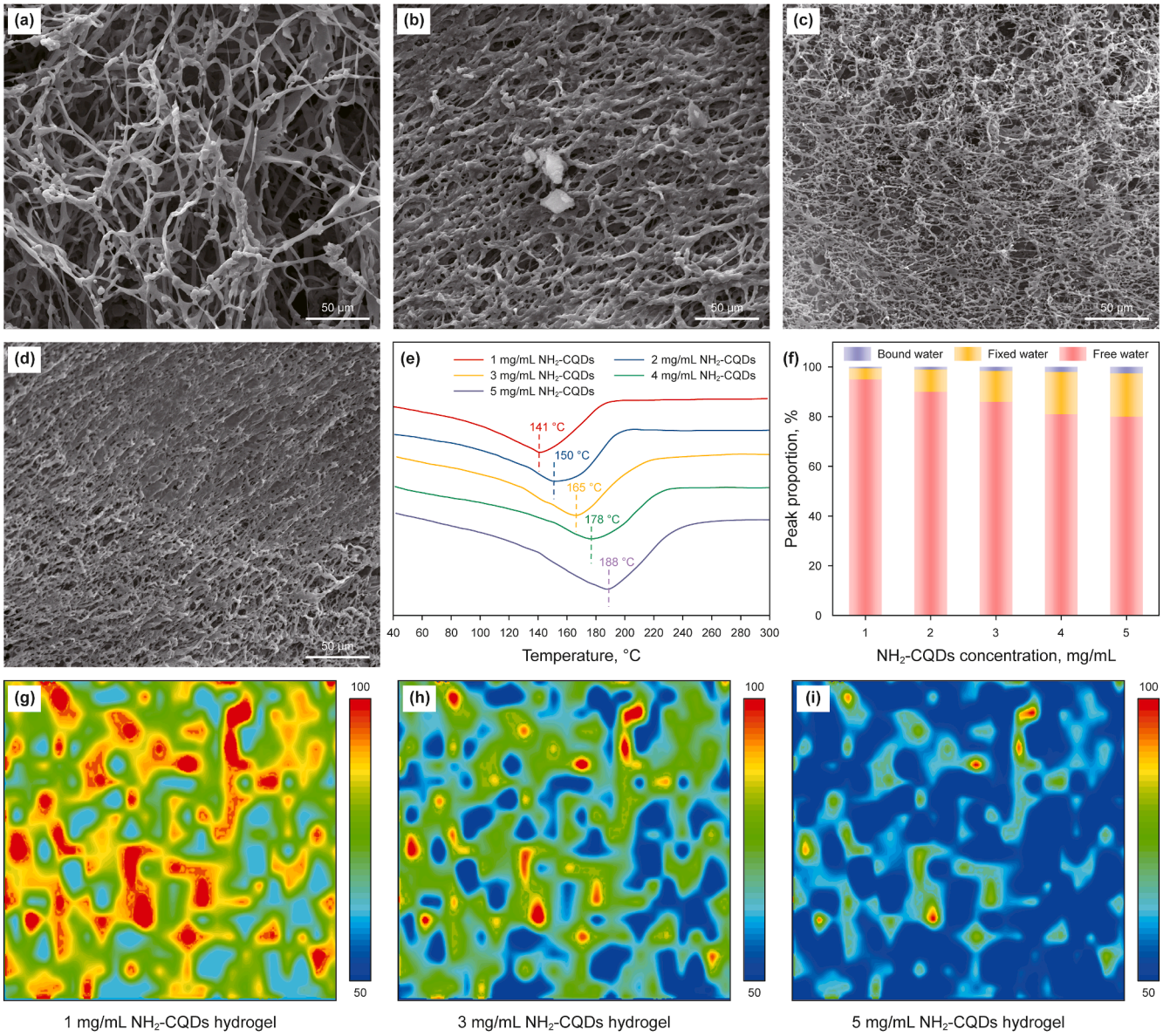

Fig. 4. **(a)** SEM images of polymers, **(b)** SEM images of hydrogels with 1 mg/mL NH_2-CQDs, **(c)** SEM images of hydrogels with 3 mg/mL NH_2-CQDs, **(d)** SEM images of hydrogels with 5 mg/mL NH_2-CQDs, **(e)** DSC images of hydrogels with different NH_2-CQDs concentrations, **(f)** LF NMR spectra of hydrogels with different NH_2-CQDs concentrations, two-dimensional (2D) Raman images of hydrogels with **(g)** 1 mg/mL NH_2-CQDs, **(h)** 3 mg/mL NH_2-CQDs, **(i)** 5 mg/mL NH_2-CQDs.

(d)), respectively. With the increase of NH_2-CQDs concentration, the three-dimensional network structure of the synthesized hydrogels becomes denser and more compact, the pore size of the pore structure gradually decreases. This is because the concentration of NH_2-CQDs increases, as a crosslinking agent, it provides more crosslinking sites for the crosslinking reaction, increases the crosslinking density, makes the network structure tighter, and at the same time acts as a reinforcing agent to enhance the strength of the network skeleton. Fig. 4(e) shows the DSC curve of hydrogels synthesized with different contents of NH_2-CQDs. With the increase of NH_2-CQDs concentration, the temperature resistance performance of the synthesized hydrogels is enhanced, and when NH_2-CQDs is 5 mg/L, the peak value of the DSC curve of the hydrogel is 188 °C. The mechanism by which NH_2-CQDs enhances the temperature resistance of hydrogels mainly lies in two aspects. Firstly, NH_2-CQDs acts as a crosslinking agent to increase the crosslinking opportunities and density in the hydrogel system. Secondly, NH_2-CQDs interacts with polymer radicals through hydrogen bonds, which can significantly reduce the dehydration of the hydrogel gel system and improve the temperature resistance of the hydrogel (Suleymanov and Shovgenov, 2021). The free water content of hydrogels synthesized by NH_2-CQDs with different contents was determined by low field nuclear magnetism, as shown in Fig. 4(f). With the increase of NH_2-CQDs concentration, the bound water and fixed water in the hydrogel increased, while the free water decreased, which further proved that increasing the concentration of NH_2-CQDs increased the crosslinking density and limited the movement of free water in the hydrogel. Two-dimensional (2D) Raman images of hydrogels synthesized with the same content of NH_2-CQDs were compared, as shown in Fig. 4 (g)–(i), where the blue-green region represents a higher crosslinking density, while the red-yellow region represents the opposite (Wang et al., 2024b). It was found that with the increase of NH_2-CQDs concentration, hydrogels exhibited greater

cross-linking density, as observed in Fig. 4(a)–(d). This was due to the increase of NH_2-CQDs concentration, the number of cross-linking sites with PAM was increased, and the network structure formed was closer.

3.3. Mechanical properties of hydrogels

As a kind of flexible material, hydrogel should have good mechanical properties in the process of environmental application. The mechanical and cyclic properties of PANC hydrogel were tested by universal testing machine to measure the influence of NH_2-CQDs on the properties of hydrogel. Fig. 5(a) shows the stress-strain curves of NH_2-CQDs hydrogels with different mass concentrations under tensile mode. Fig. 5(b) shows the histograms of fracture stress and elongation at break of NH_2-CQDs hydrogels with different mass concentrations. Among them, the tensile strain of 4 mg/mL NH_2-CQDs hydrogel can reach 368%, which is much higher than that of hydrogels with other concentrations of NH_2-CQDs. Although the fracture stress of 4 mg/mL NH_2-CQDs hydrogel is not optimal, combined with the Young's modulus and toughness histogram in Fig. 5(c), The hydrogel of 4 mg/mL NH_2-CQDs has the best Young's modulus (96 kPa) and toughness (49.6 kJ/m^3), so the hydrogel of 4 mg/mL NH_2-CQDs has the best comprehensive mechanical properties. With the increase of NH_2-CQDs concentration, the tensile strength of hydrogel increases gradually due to the covalent bond formed by PAM reaction with NH_2-CQDs and the hydrogen bond between hydrogel and NH_2-CQDs, but the tensile strain increases first and then decreases. This indicates that the hydrogels prepared with appropriate concentration of NH_2-CQDs have excellent elongation at break and mechanical stability, because the amino group on the surface of NH_2-CQDs and the amino group of PAM undergo transamidation reaction to form covalent bonds, and a large number of hydroxyl and carboxyl groups on the surface of NH_2-CQDs can form hydrogen bonds with the hydrogels, which has the effect of improving the hydrogel strength. When the concentration of NH_2-CQDs in the

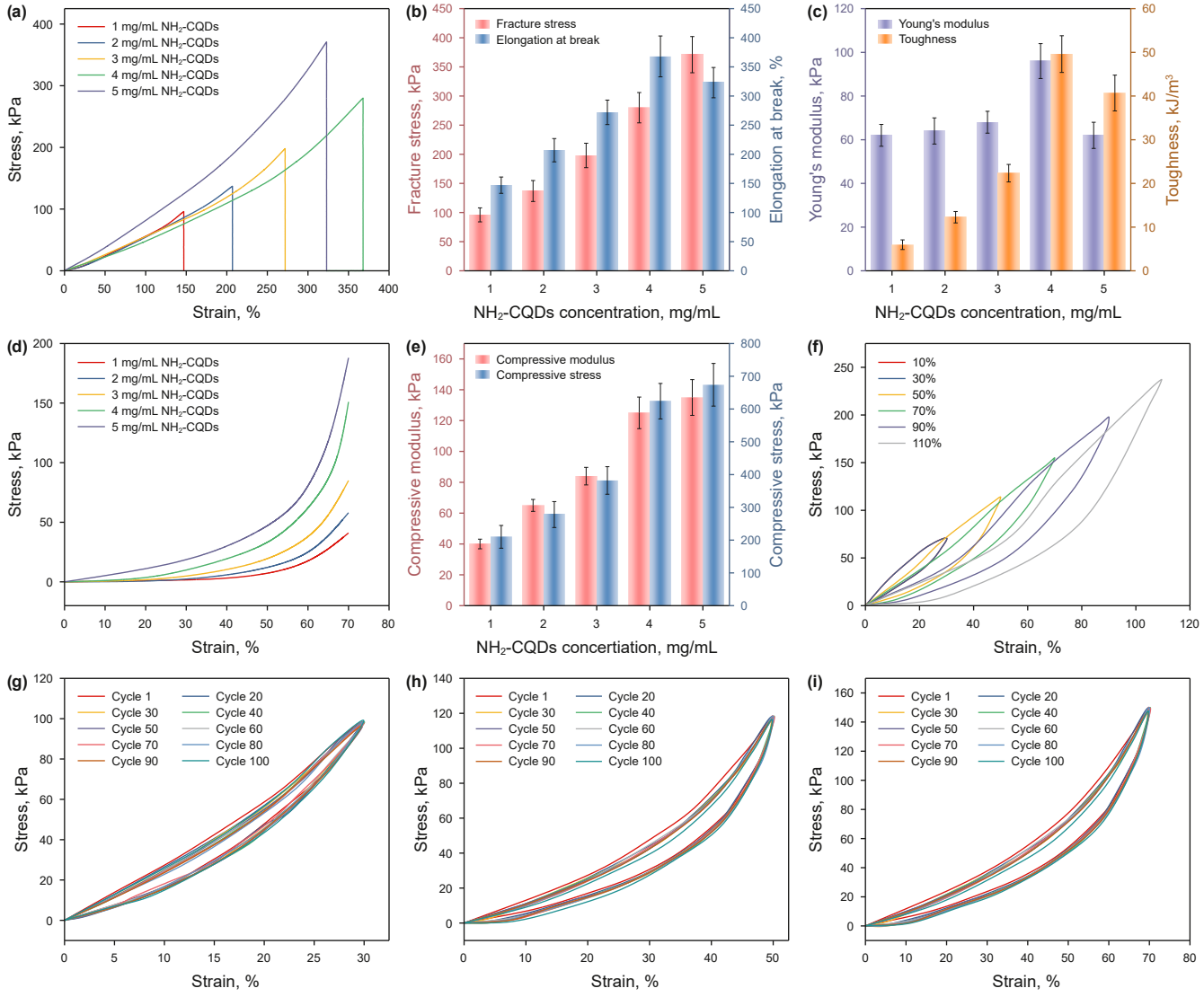

Fig. 5. Mechanical properties and stability of hydrogels. **(a)** Stress-strain curves of NH_2-CQDs hydrogels with different concentrations, **(b)** histograms of fracture stress and elongation at break of NH_2-CQDs hydrogel with different mass concentrations, **(c)** histogram of Young's modulus and toughness of NH_2-CQDs hydrogels with different mass concentrations, **(d)** stress-strain curves of NH_2-CQDs hydrogels with different mass concentrations under compression mode, **(e)** histogram of compressive modulus and compressive stress of NH_2-CQDs hydrogels with different mass concentrations, **(f)** loading and unloading curves of 4 mg/mL NH_2-CQDs hydrogel under different strains, 100 stretching cycles of 4 mg/mL NH_2-CQDs hydrogel at **(g)** 30%, **(h)** 50%, and **(i)** 70%.

hydrogel exceeds 4 mg/mL, although the crosslinking density increases, the structure of the hydrogel is eventually destroyed due to water absorption and swelling, so the tensile strength increases and the tensile strain decreases. Fig. 5(d) shows the stress-strain curve of NH_2-CQDs hydrogels with different mass concentrations under compression mode, and Fig. 5(e) shows the compression modulus and compressive stress histogram of NH_2-CQDs hydrogels with different mass concentrations. With the increase of NH_2-CQDs concentration, the compression modulus and compressive stress of hydrogel gradually increase, which is due to the increase of NH_2-CQDs concentration, the increase of crosslinking density, the enhancement of hydrogel network structure, and the improvement of its compression performance. Although the compression modulus and compressive stress of 4 mg/mL NH_2-CQDs hydrogel are not the largest, the improvement of the compression performance of hydrogel by 5 mg/mL NH_2-CQDs is not obvious compared with 4 mg/mL NH_2-CQDs. We believe that 4 mg/mL NH_2-CQDs hydrogel has the best mechanical properties. Fig. 5(f) shows the loading and unloading curves of 4 mg/mL NH_2-CQDs hydrogel under different strains, and the mechanical properties of the hydrogel remain good after the end of the stretching cycle. Fig. 5(g), (h), and (i) show the tensile cycles of 4 mg/mL NH_2-CQDs hydrogel at 30%, 50%, and 70% strain, and the hydrogel maintains good tensile properties after 100 cycles.

3.4. Rheological properties of PANC hydrogels

To verify the shear resistance and adhesion of the hydrogels, the rheological properties of the hydrogels were tested by high temperature Harker rheometer and universal testing machine, and the structural strength of the hydrogels was characterized by steady state and dynamic shear of the hydrogels. As shown in Fig. 6 (a) and (b), with the increase of shear stress, there exists a linear viscoelastic region in the hydrogel, and the storage modulus is always greater than the loss modulus at the same NH_2-CQDs concentration. This indicates that the hydrogel is mainly elastic and is a gel-like substance. As the NH_2-CQDs concentration increases, the linear viscoelastic interval range of the hydrogel becomes larger, and the storage modulus and loss modulus increase. This is because the concentration of NH_2-CQDs as a crosslinking

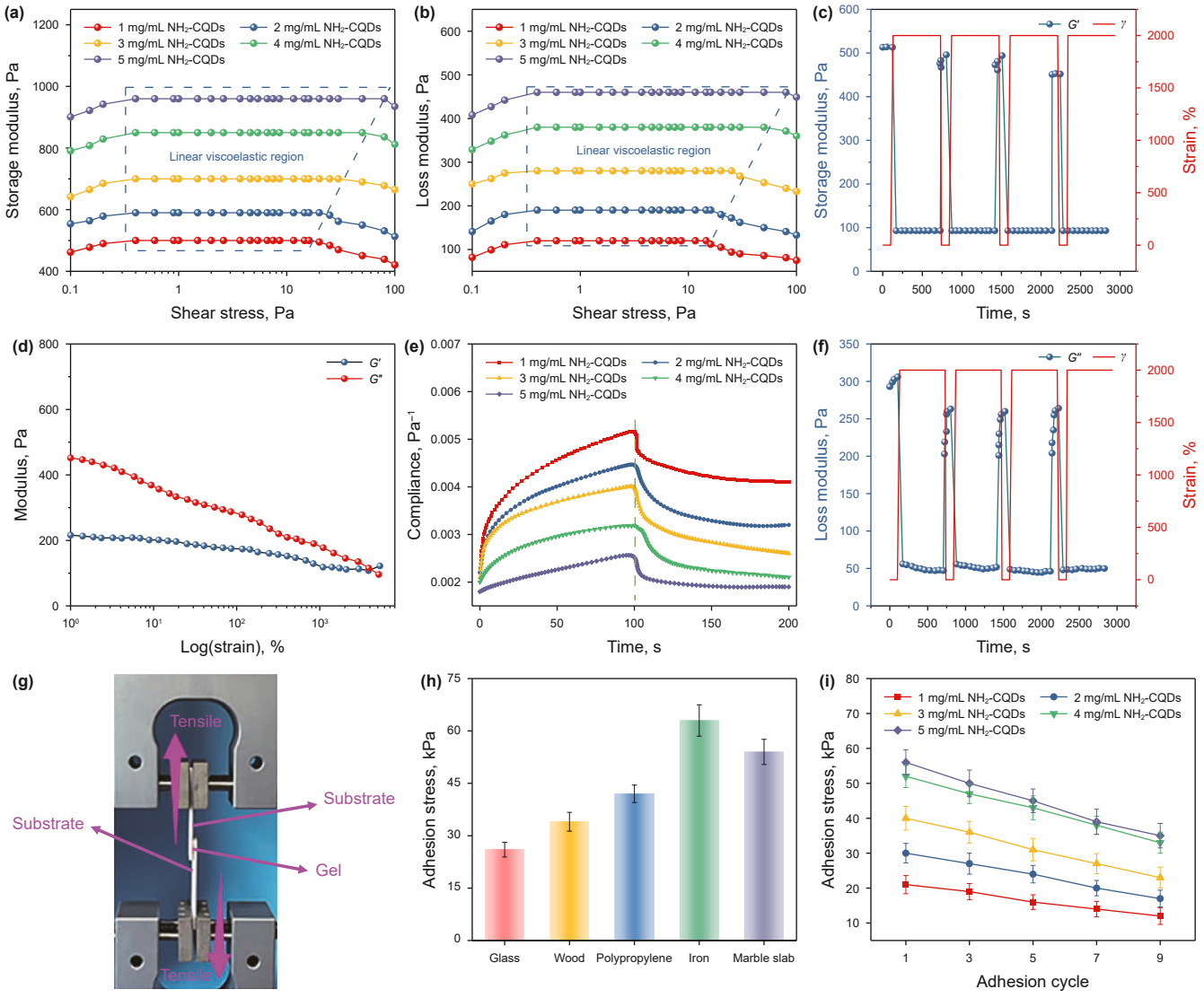

Fig. 6. **(a)** Storage modulus-stress scanning diagram of hydrogel, **(b)** loss modulus-stress scanning diagram of hydrogel, **(c)** and **(f)** the multi-period strain oscillation scanning curve of gel, **(d)** stress scans of hydrogels, **(e)** creep-recovery diagram of hydrogels, **(g)** adhesion test diagram, **(h)** histogram of adhesion of different substrates, **(i)** changes in the adhesion strength of hydrogels under different adhesion cycles.

agent increases, the crosslinking density increases, and at the same time, the hydrogen bond interaction between NH_2-CQDs and the polymer chain is enhanced, the network structure of the hydrogel is strengthened, and the viscoelasticity is enhanced. When the concentration of NH_2-CQDs is 5 mg/L, the storage modulus and loss modulus of the hydrogel can reach 960 and 460 Pa, respectively. In terms of the viscoelastic performance of other enhanced oil recovery hydrogels, under the condition of not adding reinforcing agents, the storage modulus and loss modulus of most enhanced oil recovery hydrogels are lower than 900 and 200 Pa, respectively (Kang et al., 2025; Song et al., 2023; Zhang et al., 2020b), which shows the advantage of NH_2-CQDs as a hydrogel crosslinking agent in viscoelastic properties. As the strain continues to increase, the modulus of the gel continues to decrease, and the G' and G'' curves intersect, indicating that a serious dislocation of the polymer chain occurs outside this critical strain point and the polymer network is broken (Xu et al., 2024), and the critical strain point of hydrogel is about 1350%. The shear strain values of 10% and 2000% were selected for multi-period strain oscillation scanning. The modulus recovery rate of the gel after repeated shear is shown in Fig. 6(c) and (f). After high strain (2000%) shear, the G' of gels decreased to different degrees. After three times of high strain shear, the G' of hydrogel decreased from 512–515 Pa to 451–455 Pa, and the G' recovery was about 88.35%. The G'' of the gel decreased from 293–306 Pa to 255–264 Pa, and the G'' recovery was about 86.27%. The hydrogel prepared in this study is a cross-linked system with NH_2-CQDs with high hydroxyl content as the cross-linking agent. Multi-period strain oscillation scanning proves that its self-healing property has a good effect on fluid shear in reservoir pores. Creep-resilience indicates the viscosity and elastic response of a gel sample under certain stress conditions. Fig. 6(e) shows the influence of NH_2-CQDs at different concentrations on the creep-recovery performance of the gel system. In the creep stage of the gel system (0–100 s), the compliance of the hydrogel system with different concentrations of NH_2-CQDs presents a rising trend under the influence of stress. In the recovery stage (100–200 s), after the stress is withdrawn, the hydrogel system with NH_2-CQDs concentration less than 4 mg/mL could not completely recover, while the gel system with 4 mg/mL and 5 mg/mL NH_2-CQDs could completely recover. This shows that increasing the concentration of NH_2-CQDs can improve the creep recovery performance of the gel system, and at the same time, increasing the concentration of NH_2-CQDs reduces the compliance value of the system. The lower the compliance of the system, the relatively high strength of the system, so it is not easy to deform, and it is easier to return to the original state after deformation, which is close to the ideal solid response, so that it has a good effect on the fluid impact in the reservoir pores.

In order to quantify the adhesive properties of hydrogels to different substrates, stretch-shear was used to test the adhesive strength of hydrogels. Fig. 6(g) is a schematic diagram of sample adhesion tested by stretch-shear. Fig. 6(h) shows that hydrogel has good adhesion to glass, wood, iron sheet, polypropylene plastic, marble and other substrates, among which the adhesion of hydrogel to metal iron is the largest, because when the gel adheres to some metals (such as iron, copper, aluminum and other metals) or the substrate containing metal ions, the C=O group in polyacrylamide can form a metal complex with it at the interface. Secondly, hydrogen bonding is also an important factor that cannot be ignored. The large number of hydroxyl groups contained on the surface of NH_2-CQDs and the C=O in the gel network can form hydrogen bonds with the substrates containing –OH groups (or other functional groups containing N, O and F). In addition, the intermolecular Van der Waals forces are also conducive to the adhesion of hydrogels to the surface of metal substrates. However, for organic matter, the weak interaction such as hydrogen bond and Van der Waals force plays a dominant role in adhesion, and marble contains rich functional groups containing O, which is also the gel has a large adhesion to the marble substrate. For metal substrates, in addition to hydrogen bonds, there are metal coordination, which is caused by the synergistic effect of the two. In order to further verify the repeatability of adhesion, nine cyclic stretching-shear tests were carried out on the marble slabs (Fig. 6(i)). As the concentration of NH_2-CQDs increased, the adhesive force increased, which was caused by the formation of a large number of hydrogen bonds between the surface of NH_2-CQDs and the surface of marble slabs. The adhesion of hydrogels decreased slightly with the increase of the number of cycles, but it still met the adhesion requirements of hydrogels.

3.5. Intelligent response of hydrogel

The intelligent responsiveness of micro-nano capsules was evaluated by measuring the gelation time of hydrogels at different temperatures and pH values. The non-encapsulated hydrogels were named PANC, while the hydrogels encapsulated with 5%, 8% and 10% hydrophobic SiO_2 were named PANC1, PANC2 and PANC3, respectively. The experimental results were shown in Fig. 7. Fig. 7(a) shows that when pH = 7, the capsulized hydrogel has a longer gelation time and the greater the content of hydrophobic SiO_2, the longer the gelation time. This is because the increase of the content of hydrophobic SiO_2, more hydrophobic particles participate in the self-assembly process, and the stability of micro-nano capsules is enhanced (Panthi et al., 2017). For PANC3, at 90, 110, 130, 150, 170 °C, the gelation time of encapsulated hydrogel was 16, 17.3, 24, 40, 44 times that of unencapsulated hydrogel. This indicates that the encapsulated hydrogel can effectively delay the occurrence of crosslinking reaction at high temperature, and greatly prolong the gelation time of hydrogel at high temperature. Fig. 7(b) shows that at 170 °C, the change of pH has little effect on the gelation time of PANC, but for the encapsulated hydrogel, the gelation time of the encapsulated hydrogel is shortened with the increase of pH value. The analysis is that the acidic condition is conducive to the formation of micro-nano capsules in aqueous solution of gaseous hydrophobic SiO_2, and the increase of pH value will increase the charge number on the surface of the hydrophobic SiO_2 nanoparticles, reduce their hydrophobic properties (Singh et al., 2017), and lead to the decline of self-assembly, thus prolongating the effect of gelation time. Micro-nano capsules can achieve intelligent responses through temperature and pH changes, in which the pH response essentially changes the hydrophobic properties of hydrophobic particles. Inspired by this, surface activators are often used to change rock wettability. Fig. 7(c) and (d) respectively shows the effects of adding anion surfactant α-alkenyl sulfonate (AOS) with different mass fractions on the gelation time of hydrogels at 140 °C and pH = 7. The experiment shows that adding AOS surfactant to the encapsulated hydrogel system can, to a certain extent, disrupt the encapsulation of hydrophobic SiO_2 nanoparticles and weaken the effect of the encapsulated hydrogel in delaying the gelation time. The main reason is that the increase in the concentration of surfactant in the solution will reduce the air-water contact Angle and enhance the surface hydrophilicity. This leads to a deterioration in the self-assembly effect of hydrophobic SiO_2 nanoparticles.

3.6. Mechanism of underground hydrogel regulating and flooding

As shown in Fig. 8, (a) is the distribution of oil in the saturated oil state of the glass model, and Fig. 8(b) is the microscope enlarged image of oil phase distribution in the model. It can be

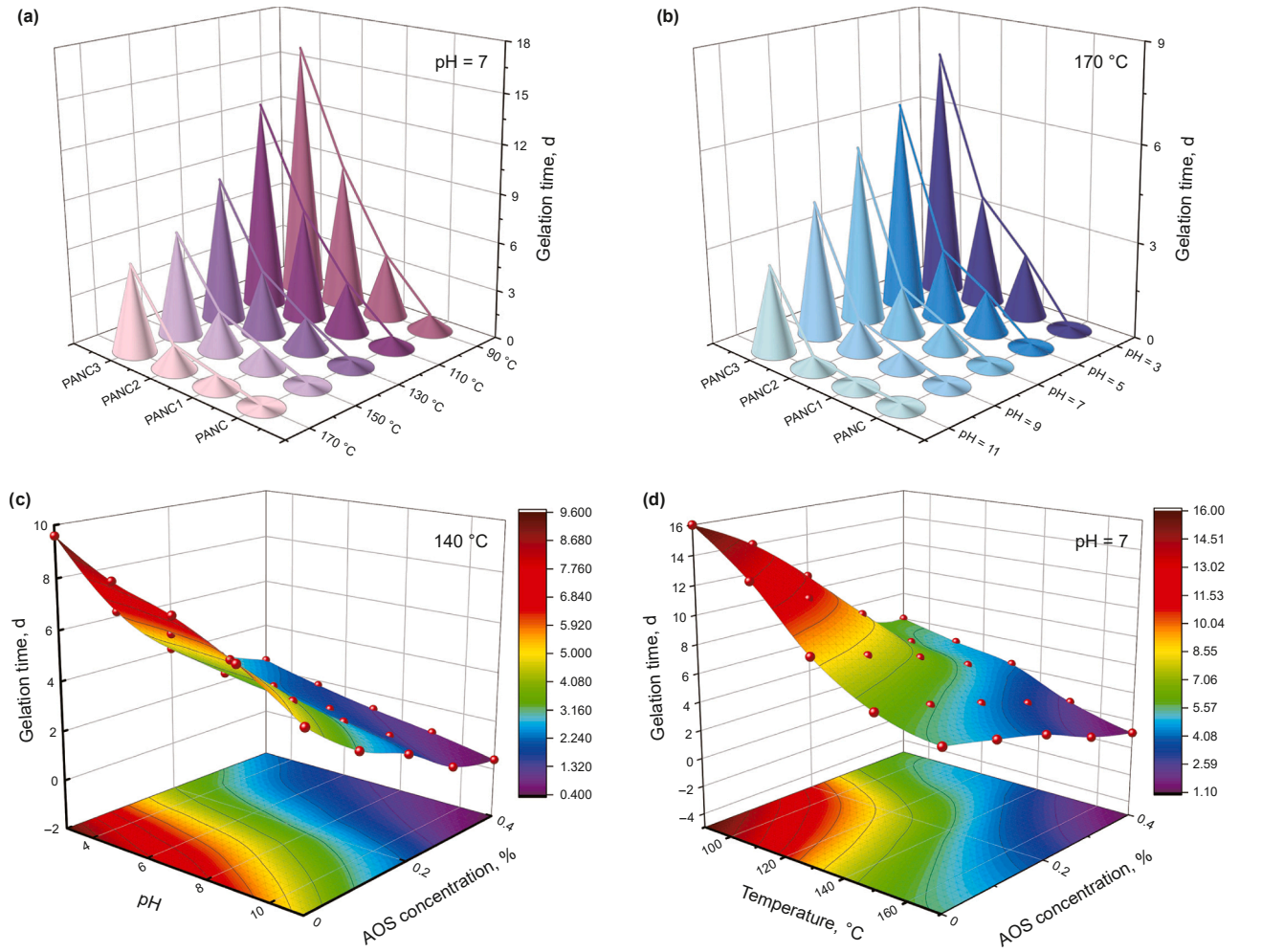

Fig. 7. **(a)** Effect of hydrophobic SiO_2 on the gelation time of encapsulated hydrogel when pH = 7, **(b)** effect of pH on the gelation time of hydrogel at 170 °C, **(c)** effect of adding AOS with different mass fraction on the formation time of hydrogel at 140 °C, and **(d)** pH = 7.

clearly seen that the void in the model is filled with oil phase, and the saturated oil area accounted for 77.74% of the microscopic model area by using image J software. Fig. 8(c) shows the two-phase distribution of oil and water in the model after a primary water flooding and Fig. 8(d) shows the microscope enlarged image of the two-phase distribution of oil and water after a primary water flooding. It can be clearly seen that a dominant flow channel (red dashed line) has been formed in the model, and part of the oil phase has been injected and displaced by water, but there is still a large amount of oil in the pores that has not been swept by injected water. The remaining oil area accounts for 56.88% of the microscopic model area, and the primary water flooding efficiency is 20.86%. Fig. 8(e) shows the three-phase distribution of oil, water and base liquid after the injection of hydrogel base liquid (blue). Part of the oil phase continues to be displaced by hydrogel base liquid, and the remaining oil decreases compared with that after water flooding, but there is still more remaining oil. Fig. 8(f) shows the microscope enlarged image of the distribution of oil, water and base liquid after injection of hydrogel base solution. It can be seen through microscope that the original water dominant channel inside the model is occupied by the hydrogel base solution (blue channel), which indicates that the hydrogel base solution mainly moves along the dominant water channel generated by water flooding before injection, displacing the remaining water and occupying the water channel. At this time, the remaining oil area accounts for 49.71% of the area of the microscopic model. Fig. 8(g) shows the oil-water distribution after secondary water flooding. Compared with primary water flooding, it can be clearly seen that the flow channels of secondary water flooding are significantly increased, and the spread range of water flooding is larger. Fig. 8(h) shows the microscope magnification image of oil-water distribution after secondary water flooding, and it can be seen that the water channel generated by primary water flooding is blocked by gel, and new water channel is generated by secondary water flooding. The remaining oil area accounts for 31.04% of the microscopic model area, and the oil recovery factor increased by 18.67%. In previous studies on enhanced oil recovery by hydrogels, the in-situ cross-linked weak gel developed by Yin et al. (2022) could enhance the oil recovery by 12.4%. Jia et al. (2024) evaluated that the recovery rate of the phenol-formaldehyde cross-linked gel system was 15.7%, and that of the PEI cross-linked gel system was 14.1%. The nanocomposite gel developed by Zhang et al. (2025) can enhance the oil recovery by up to 16.4%. The enhanced oil recovery of these hydrogels is all lower than those of the hydrogels we introduced, which shows the advantages of this hydrogel in enhancing oil recovery.

The regulating and flooding mechanism of hydrogel is as follows: by blocking the dominant flow channel after primary water

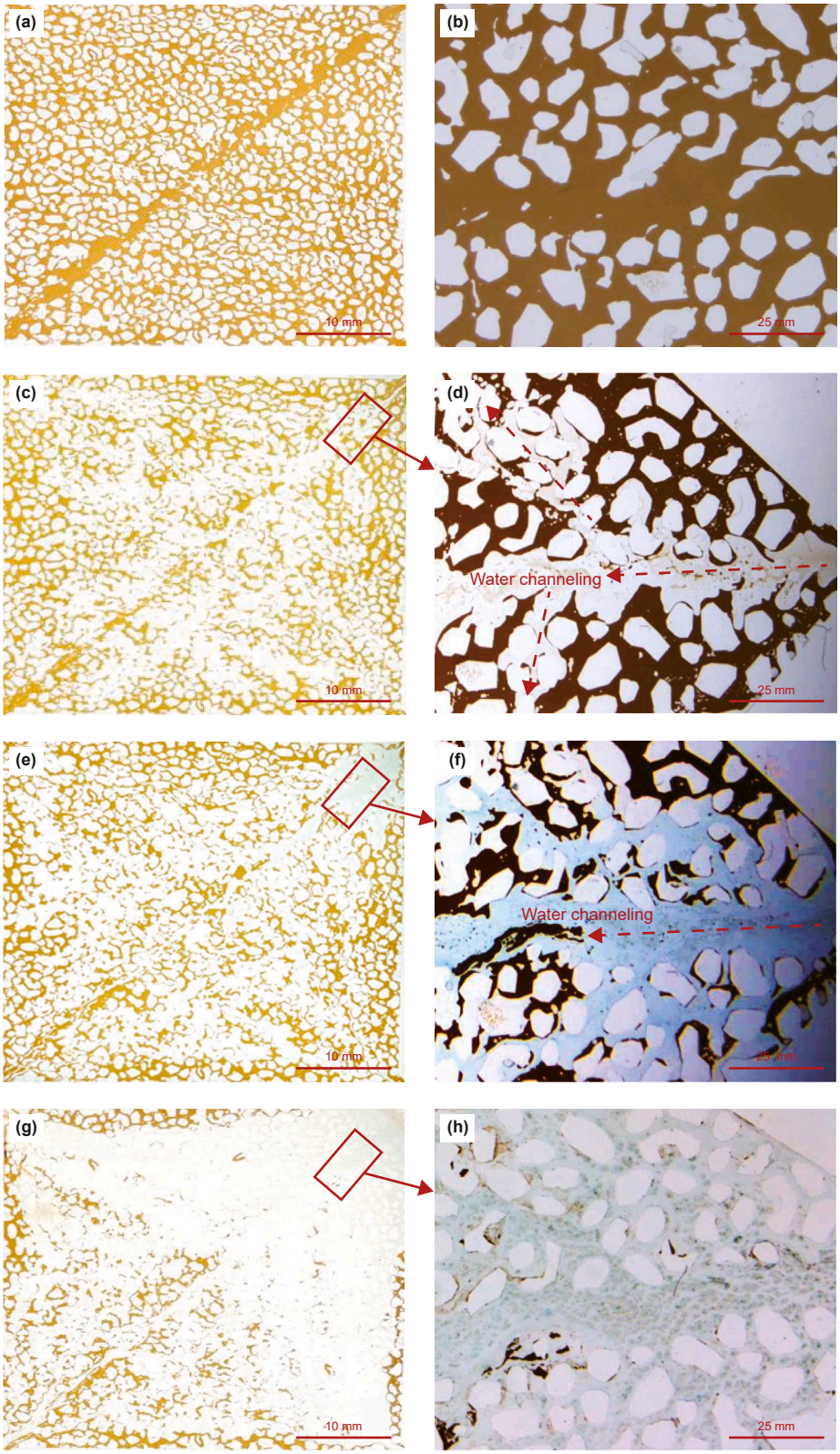

Fig. 8. **(a)** Oil distribution in the saturated oil state of the glass model, **(b)** microscope enlarged image of the oil phase distribution in the model, **(c)** two-phase distribution of oil and water in the model after a primary water flooding, **(d)** microscope magnification of oil-water two-phase distribution after a primary water flooding, **(e)** three-phase distribution of oil, water, and base solution after injection of hydrogel base solution (blue), **(f)** microscopically magnified images showing the three-phase distribution of oil, water, and base liquid after injection of the hydrogel base solution, **(g)** oil-water distribution after secondary water flooding, **(h)** microscope magnification image of oil-water distribution after secondary water flooding.

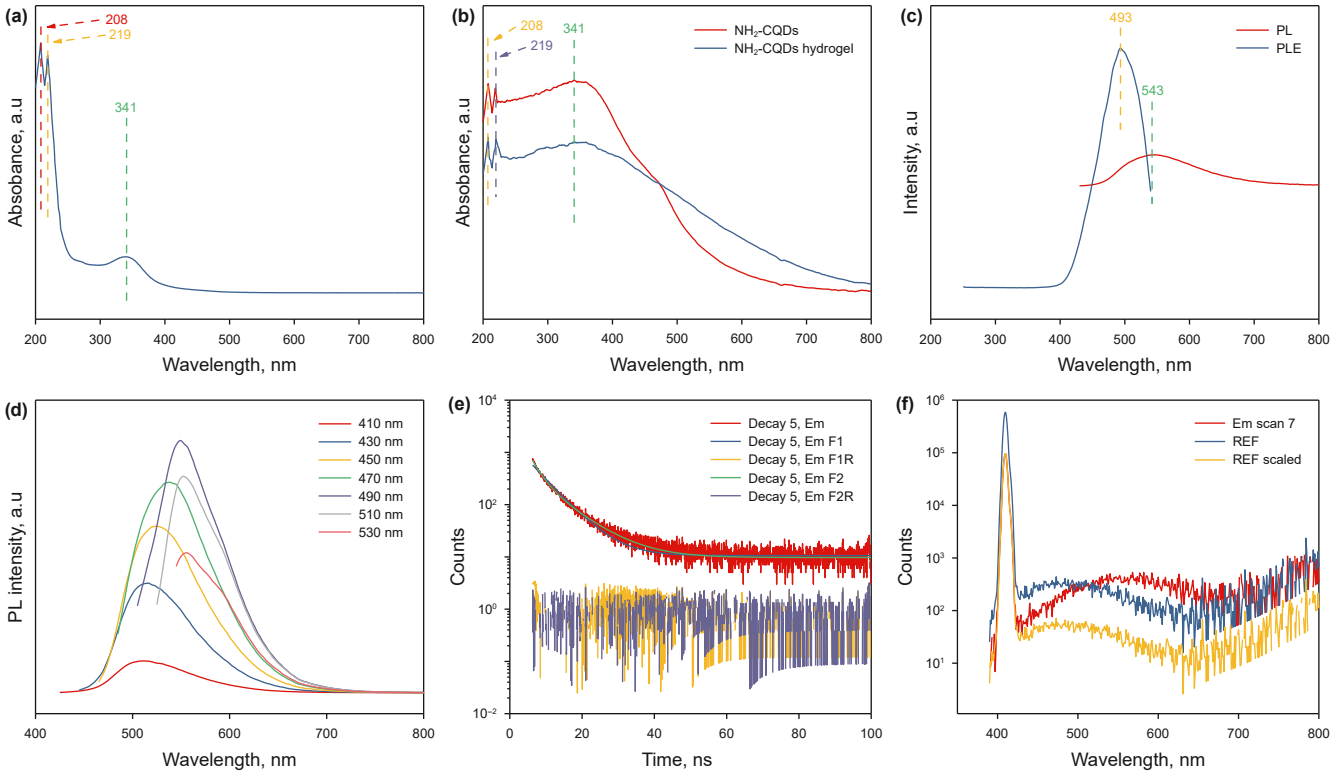

Fig. 9. **(a)** UV-vis diffuse reflectance spectrum, **(b)** PL and PLE spectra of NH_2-CQDs, **(c)** PL and PLE spectra of NH_2-CQDs hydrogels, **(d)** PL emission spectrum of NH_2-CQDs, **(e)** PL lifetime data of NH_2-CQDs, **(f)** fluorescence yield curve of NH_2-CQDs.

flooding and adjusting the flow channel of secondary water flooding, the spread range of secondary water flooding is increased and the recovery rate is further improved.

3.7. Underground signal tracking

Carbon quantum dots emit different colors of light under ultraviolet light, so they are more stable and tunable than other fluorescent materials and are often used to design fluorescence sensors. When hydrogels are applied to underground flow control, hydrogels flow in formation cracks or artificial cracks without human control and detection, while PANC hydrogels are synthesized hydrogels based on NH_2-CQDs and have the fluorescence characteristics of NH_2-CQDs. After PANC hydrogels are injected underground, fluorescence of flowback fluid can be detected in adjacent wells to determine well group connectivity and underground fracture structure. Therefore, we studied the fluorescence characteristics of NH_2-CQDs and PANC hydrogels.

Fig. 9(a) shows the solid UV-visible diffuse spectra of NH_2-CQDs powder and hydrogel powder. NH_2-CQDs with strong absorption peaks mainly appear in the ultraviolet region (200–345 nm), and NH_2-CQDs has absorption peaks at 208, 219 and 341 nm, respectively. This suggests that NH_2-CQDs has absorption capacity over a wide wavelength range of 200–400 nm, with strong adsorption peaks below 300 nm generally attributed to the n-π* transition of the conjugated C=O bonds (Huang et al., 2021), and specific absorption peaks at 341 nm attributed to nitrogen-doped CQD. Due to the presence of NH_2 on the nitrogen-doped CQD surface, the conjugation of the entire system increases, and the π-π* transition of the C=O bond redshifts to 341 nm (Wei et al., 2023). NH_2-CQDs hydrogels have the same peak position, which further confirms that NH_2-CQDs crosslinks with PAM to form hydrogels. Fig. 9(b) shows that the PL spectrum of NH_2-CQDs shows a maximum emission peak of about 543 nm when excited at 493 nm, while Fig. 9(c) shows that the PL spectrum of NH_2-CQDs hydrogel shows a maximum emission peak of about 488 nm when excited at 400 nm. It is confirmed that NH_2-CQDs endows hydrogels with fluorescence properties, which will achieve underground tracking of NH_2-CQDs hydrogels. Fig. 9(d) shows that as the excitation wavelength increases from 410 to 530 nm, the emission peak of NH_2-CQDs gradually redshifts from 510 to 557 nm. It can be clearly observed that when the excitation wavelength is 490 nm, the emission wavelength of NH_2-CQDs reaches a maximum, which is almost exactly consistent with the result of Fig. 9(b), and then the fluorescence intensity gradually decreases with the change of excitation wavelength. Fig. 9(e) shows PL decay and double exponential fitting curves for NH_2-CQDs. Therefore, according to Eq. (2) in Supplementary Information, the average fluorescence lifetime is calculated to be 6.50 ns, which is suitable for fluorescence detection. Fig. 9(f) shows the fluorescence yield curve of NH_2-CQDs, and the fluorescence quantum yield (QY) of NH_2-CQDs is 2.37%.

4. Conclusion

In this work, we synthesized amino functionalized carbon quantum dots (NH_2-CQDs) using glucose as a precursor in a simple step. NH_2-CQDs can not only act as a chemical crosslinking agent of hydrogels, but also as a physical enhancer, and NH_2-CQDs hydrogel can remain stable at 170 °C for 300 days and has high tensile strength (371 kPa), good toughness (49.6 kJ/m^3), excellent viscoelasticity ($G' = 960$ Pa, $G'' = 460$ Pa), shear resistance and adhesion properties. At the same time, micro-nano capsules containing NH_2-CQDs are formed by the self-assembly of hydrophobic SiO_2 on water droplets, and the NH_2-CQDs solution is released by the capsule under external conditions (temperature, pH value,

surfactant). This method greatly delays the crosslinking time between the polymer and the crosslinking agent at high temperature. The gelation time of the hydrogel encapsulated with 10% hydrophobic SiO_2 at 170 °C and pH = 7 is 44 times that of the unencapsulated hydrogel. In short, we have developed an intelligent response micro-nano capsule hydrogel based on NH_2-CQDs. The hydrogel has good mechanical properties and rheological properties, and can control the gelation time of the hydrogel through intelligent response to achieve deep underground flow control, and the fluorescence characteristics of the hydrogel given by NH_2-CQDs can also help realize underground signal tracking. It has a potential application prospect in the field of underground flow control.

CRediT authorship contribution statement

Chuan-Hong Kang: Writing – original draft, Investigation, Conceptualization, Methodology, Data curation. **Ji-Xiang Guo:** Supervision, Project administration, Funding acquisition, Writing – review & editing, Resources. **Zheng-Hao Zhang:** Investigation, Methodology. **Wyclif Kiyingi:** Methodology. **Peng-Cheng Xue:** Resources.

Data availability

Data will be made available on request.

Declaration of competing interest

The authors declare that they have no known competing financial interests or personal relationships that could have appeared to influence the work reported in this paper.

Acknowledgements

This study received support and funding from the National Natural Science Foundation of China (No. 52174047).

Appendix A. Supplementary data

Supplementary data to this article can be found online at https://doi.org/10.1016/j.petsci.2025.09.032.

References

Bertsch, P., Diba, M., Mooney, D.J., et al., 2023. Self-healing injectable hydrogels for tissue regeneration. Chem. Rev. 123 (2), 834–873. https://doi.org/10.1021/acs.chemrev.2c00179.

Campea, M.A., Majcher, M.J., Lofts, A., et al., 2021. A review of design and fabrication methods for nanoparticle network hydrogels for biomedical, environmental, and industrial applications. Adv. Funct. Mater. 31 (33), 2102355. https://doi.org/10.1002/adfm.202102355.

Cao, G., Zhao, L., Ji, X., et al., 2023. "Salting out" in hofmeister effect enhancing mechanical and electrochemical performance of amide-based hydrogel electrolytes for flexible zinc-ion battery. Small 19 (30), 2207610. https://doi.org/10.1002/smll.202207610.

Clasky, A.J., Watchorn, J.D., Chen, P.Z., et al., 2021. From prevention to diagnosis and treatment: biomedical applications of metal nanoparticle-hydrogel composites. Acta Biomater. 122, 1–25. https://doi.org/10.1016/j.actbio.2020.12.030.

Ding, H., Xin, Z., Yang, Y., et al., 2020. Ultrasensitive, low-voltage operational, and asymmetric ionic sensing hydrogel for multipurpose applications. Adv. Funct. Mater. 30 (12), 1909616. https://doi.org/10.1002/adfm.201909616.

Đorđević, L., Arcudi, F., Cacioppo, M., et al., 2022. A multifunctional chemical toolbox to engineer carbon dots for biomedical and energy applications. Nat. Nanotechnol. 17 (2), 112–130. https://doi.org/10.1038/s41565-021-01051-7.

Đorđević, L., Arcudi, F., Prato, M., 2019. Preparation, functionalization and characterization of engineered carbon nanodots. Nat. Protoc. 14 (10), 2931–2953. https://doi.org/10.1038/s41596-019-0207-x.

Edwards, R.W.J., Celia, M.A., 2018. Infrastructure to enable deployment of carbon capture, utilization, and storage in the United States. Proc. Natl. Acad. Sci. 115 (38), E8815–E8824. https://doi.org/10.1073/pnas.1806504115.

Guimarães, C.F., Ahmed, R., Marques, A.P., et al., 2021. Engineering hydrogel-based biomedical photonics: design, fabrication, and applications. Adv. Mater. 33 (23), 2006582. https://doi.org/10.1002/adma.202006582.

Guo, Y., Bae, J., Fang, Z., et al., 2020. Hydrogels and hydrogel-derived materials for energy and water sustainability. Chem. Rev. 120 (15), 7642–7707. https://doi.org/10.1021/acs.chemrev.0c00345.

Huang, J., Liu, X., Li, L., et al., 2021. Nitrogen-doped carbon quantum dot-anchored hydrogels for visual recognition of dual metal ions through reversible fluorescence response. ACS Sustain. Chem. Eng. 9 (45), 15190–15201. https://doi.org/10.1021/acssuschemeng.1c04521.

Jayakumar, A., Jose, V.K., Lee, J., 2020. Hydrogels for medical and environmental applications. Small Methods 4 (3), 1900735. https://doi.org/10.1002/smtd.201900735.

Jia, H., Wu, J., Wu, S., et al., 2024. New insights into the DPR mechanism of elastic energy released by polymer gel for enhanced oil recovery. Petroleum 10 (3), 539–547. https://doi.org/10.1016/j.petlm.2022.08.002.

Jiang, Y., Krishnan, N., Heo, J., et al., 2020. Nanoparticle–hydrogel superstructures for biomedical applications. J. Contr. Release 324, 505–521. https://doi.org/10.1016/j.jconrel.2020.05.041.

Kang, C., Guo, J., Kiyingi, W., et al., 2025. A new self-healing green polymer gel with dynamic networks for flow control in harsh reservoirs. Adv. Funct. Mater. 35 (17), 2423892. https://doi.org/10.1002/adfm.202423892.

Kou, X., Jiang, S., Park, S.J., et al., 2020. A review: recent advances in preparations and applications of heteroatom-doped carbon quantum dots. Dalton Trans. 49 (21), 6915–6938. https://doi.org/10.1039/d0dt01004a.

Li, J., Gong, X., 2022. The emerging development of multicolor carbon dots. Small 18 (51), 2205099. https://doi.org/10.1002/smll.202205099.

Li, L., Meng, J., Zhang, M., et al., 2022. Recent advances in conductive polymer hydrogel composites and nanocomposites for flexible electrochemical supercapacitors. Chem. Commun. 58 (2), 185–207. https://doi.org/10.1039/D1CC05526G.

Li, X., Zhao, S., Li, B., et al., 2021. Advances and perspectives in carbon dot-based fluorescent probes: mechanism, and application. Coord. Chem. Rev. 431, 213686. https://doi.org/10.1016/j.ccr.2020.213686.

Li, Y., Rodrigues, J., Tomás, H., 2012. Injectable and biodegradable hydrogels: gelation, biodegradation and biomedical applications. Chem. Soc. Rev. 41 (6), 2193–2221. https://doi.org/10.1039/c1cs15203c.

Liu, Y., Dai, C., Wang, K., et al., 2017. Study on a novel cross-linked polymer gel strengthened with silica nanoparticles. Energy Fuel 31 (9), 9152–9161. https://doi.org/10.1021/acs.energyfuels.7b01432.

Lu, S., Bo, Q., Zhao, G., et al., 2023. Recent advances in enhanced polymer gels for profile control and water shutoff: a review. Front. Chem. 11, 1067094. https://doi.org/10.3389/fchem.2023.1067094.

Miao, Y., Xu, M., Zhang, L., 2021. Electrochemistry-induced improvements of mechanical strength, self-healing, and interfacial adhesion of hydrogels. Adv. Mater. 33 (40), 2102308. https://doi.org/10.1002/adma.202102308.

Moura, D., Pereira, A.T., Ferreira, H.P., et al., 2023. Poly(2-hydroxyethyl methacrylate) hydrogels containing graphene-based materials for blood-contact applications: from soft inert to strong degradable material. Acta Biomater. 164, 253–268. https://doi.org/10.1016/j.actbio.2023.04.031.

Mu, X., Zhou, J., Wang, P., et al., 2022. A robust starch–polyacrylamide hydrogel with scavenging energy harvesting capacity for efficient solar thermoelectricity–freshwater cogeneration. Energy Environ. Sci. 15 (8), 3388–3399. https://doi.org/10.1039/D2EE01394K.

Nele, V., Wojciechowski, J.P., Armstrong, J.P.K., et al., 2020. Tailoring gelation mechanisms for advanced hydrogel applications. Adv. Funct. Mater. 30 (42), 2002759. https://doi.org/10.1002/adfm.202002759.

Olasolo, P., Juárez, M.C., Morales, M.P., et al., 2016. Enhanced geothermal systems (EGS): a review. Renew. Sustain. Energy Rev. 56, 133–144. https://doi.org/10.1016/j.rser.2015.11.031.

Pan, X., Li, J., Ma, N., et al., 2023. Bacterial cellulose hydrogel for sensors. Chem. Eng. J. 461, 142062. https://doi.org/10.1016/j.cej.2023.142062.

Panthi, K., Singh, R., Mohanty, K.K., 2017. Microencapsulation and stimuli-responsive controlled release of particles using water-in-air powders. Langmuir 33 (16), 3998–4010. https://doi.org/10.1021/acs.langmuir.7b00149.

Park, J., Oh, Y., Jeong, S., et al., 2021. Biobased Stimuli-responsive hydrogels that comprise supramolecular interpenetrating networks and exhibit programmed behaviors. Chem. Mater. 33 (20), 8124–8132. https://doi.org/10.1021/acs.chemmater.1c02577.

Qiu, J., Liao, J., Wang, G., et al., 2022. Implanting N-doped CQDs into rGO aerogels with diversified applications in microwave absorption and wastewater treatment. Chem. Eng. J. 443, 136475. https://doi.org/10.1016/j.cej.2022.136475.

Rahmani, P., Shojaei, A., 2021. A review on the features, performance and potential applications of hydrogel-based wearable strain/pressure sensors. Adv. Colloid Interface Sci. 298, 102553. https://doi.org/10.1016/j.cis.2021.102553.

Singh, R., Panthi, K., Mohanty, K., 2017. Microencapsulation of acids by nanoparticles for acid treatment of shales. Energy Fuel 31, 11755–11764. https://doi.org/10.1021/acs.energyfuels.7b02003.

Song, T., Bai, B., Eriyagama, Y., et al., 2023. Lysine crosslinked polyacrylamide—a novel green polymer gel for preferential flow control. ACS Appl. Mater. Interfaces 15 (3), 4419–4429. https://doi.org/10.1021/acsami.2c17390.

Su, Y., Otake, K., Zheng, J., et al., 2022. Separating water isotopologues using diffusion-regulatory porous materials. Nature 611 (7935), 289–294. https://doi.org/10.1038/s41586-022-05310-y.

Suleymanov, A.B., Shovgenov, A.D., 2021. Nano composite polymer composition for water shutoff treatment at high formation temperature. In: SPE Annual

Caspian Technical Conference. SPE Annual Caspian Technical Conference. https://doi.org/10.2118/207066-ms.
Sun, T.L., Kurokawa, T., Kuroda, S., et al., 2013. Physical hydrogels composed of polyampholytes demonstrate high toughness and viscoelasticity. Nat. Mater. 12 (10), 932–937. https://doi.org/10.1038/nmat3713.
Wang, Y., Liu, K., Wei, W., et al., 2024. A multifunctional hydrogel with photothermal antibacterial and antioxidant activity for smart monitoring and promotion of diabetic wound healing. Adv. Funct. Mater. 34 (38), 2402531. https://doi.org/10.1002/adfm.202402531.
Wang, Y., Lv, T., Yin, K., et al., 2023. Carbon dot-based hydrogels: preparations, properties, and applications. Small 19 (17), 2207048. https://doi.org/10.1002/smll.202207048.
Wang, Z., Wang, S., Zhang, L., et al., 2024. Highly strong, tough, and cryogenically adaptive hydrogel ionic conductors via coordination interactions. Research 7, 298. https://doi.org/10.34133/research.0298.
Wei, X., Li, J., Hu, Z., et al., 2023. Carbon quantum dot/chitosan-derived hydrogels with photo-stress-pH multiresponsiveness for wearable sensors. Macromol. Rapid Commun. 44 (8), 2200928. https://doi.org/10.1002/marc.202200928.
Wirthl, D., Pichler, R., Drack, M., et al., 2017. Instant tough bonding of hydrogels for soft machines and electronics. Sci. Adv. 3 (6), e1700053. https://doi.org/10.1126/sciadv.1700053.
Xu, T., Liu, K., Sheng, N., et al., 2022. Biopolymer-based hydrogel electrolytes for advanced energy storage/conversion devices: properties, applications, and perspectives. Energy Storage Mater. 48, 244–262. https://doi.org/10.1016/j.ensm.2022.03.013.
Xu, Z., Zhao, M., Yang, Z., et al., 2024. Novel mussel-inspired high-temperature resistant gel with delayed crosslinking property for ultra-deep reservoir fracturing. Adv. Funct. Mater. 34 (42), 2405111. https://doi.org/10.1002/adfm.202405111.
Xue, X., Zhang, H., Liu, H., et al., 2022. Rational design of multifunctional CuS nanoparticle-PEG composite soft hydrogel-coated 3D hard polycaprolactone scaffolds for efficient bone regeneration. Adv. Funct. Mater. 32 (33), 2202470. https://doi.org/10.1002/adfm.202202470.
Yang, D., 2022. Recent advances in hydrogels. Chem. Mater. 34 (5), 1987–1989. https://doi.org/10.1021/acs.chemmater.2c00188.
Yang, F., Zhao, J., Koshut, W.J., et al., 2020. A synthetic hydrogel composite with the mechanical behavior and durability of cartilage. Adv. Funct. Mater. 30 (36), 2003451. https://doi.org/10.1002/adfm.202003451.
Yang, Q., Zhao, M., Gao, M., et al., 2021. The experimental study of silica nanoparticles strengthened polymer gel system. J. Dispersion Sci. Technol. 42 (2), 298–305. https://doi.org/10.1080/01932691.2019.1679642.
Yang, S., Tao, X., Chen, W., et al., 2022. Ionic hydrogel for efficient and scalable moisture-electric generation. Adv. Mater. 34 (21), 2200693. https://doi.org/10.1002/adma.202200693.
Yao, Y., Yin, C., Hong, S., et al., 2020. Lanthanide-ion-coordinated supramolecular hydrogel inks for 3D printed full-color luminescence and opacity-tuning soft actuators. Chem. Mater. 32 (20), 8868–8876. https://doi.org/10.1021/acs.chemmater.0c02448.
Yin, H., Yin, X., Cao, R., et al., 2022. In situ crosslinked weak gels with ultralong and tunable gelation times for improving oil recovery. Chem. Eng. J. 432, 134350. https://doi.org/10.1016/j.cej.2021.134350.
Yu, F., Yang, P., Yang, Z., et al., 2021. Double-network hydrogel adsorbents for environmental applications. Chem. Eng. J. 426, 131900. https://doi.org/10.1016/j.cej.2021.131900.
Yu, X., Zheng, Y., Zhang, H., et al., 2021. Fast-recoverable, self-healable, and adhesive nanocomposite hydrogel consisting of hybrid nanoparticles for ultrasensitive strain and pressure sensing. Chem. Mater. 33 (15), 6146–6157. https://doi.org/10.1021/acs.chemmater.1c01595.
Yuk, H., Wu, J., Zhao, X., 2022. Hydrogel interfaces for merging humans and machines. Nat. Rev. Mater. 7 (12), 935–952. https://doi.org/10.1038/s41578-022-00483-4.
Zeng, J., Jing, X., Lin, L., et al., 2025. Smart sensing hydrogel actuators conferred by MXene gradient arrangement. J. Colloid Interface Sci. 677, 816–826. https://doi.org/10.1016/j.jcis.2024.08.117.
Zhang, H., Guo, J., Wang, Y., et al., 2021. Stretchable and conductive composite structural color hydrogel films as bionic electronic skins. Adv. Sci. 8 (20), 2102156. https://doi.org/10.1002/advs.202102156.
Zhang, L., Abbaspourrad, A., Parsa, S., et al., 2020. Core-shell nanohydrogels with programmable swelling for conformance control in porous media. ACS Appl. Mater. Interfaces 12 (30), 34217–34225. https://doi.org/10.1021/acsami.0c09958.
Zhang, S., Guo, J., Gu, Y., et al., 2020. Polyacrylamide gel formed by Cr(III) and phenolic resin for water control in high-temperature reservoirs. J. Petrol. Sci. Eng. 194, 107423. https://doi.org/10.1016/j.petrol.2020.107423.
Zhang, W., Sun, Y., Meng, X., et al., 2025. Preparation and mechanism of EP-HMTA-SiO_2 nanocomposite polymer gel for enhancing oil recovery. Processes 13 (3), 596. https://doi.org/10.3390/pr13030596.
Zhu, C., Zhang, L., Zou, A., et al., 2023. A bionic intelligent hydrogel with multi-level information encryption and decryption capabilities. Chem. Eng. J. 475, 146161. https://doi.org/10.1016/j.cej.2023.146161.